ACSNANO

www.acsnano.org

Correlative and *In Situ* Microscopy Investigation of Phase Transformation, Crystal Growth, and Degradation of Antimony Sulfide Thin Films

Mingjian Wu,* Maïssa K. S. Barr, Vanessa M. Koch, Martin Dierner, Tobias Dierke, Penghan Lu, Pei-Chun Liao, Johannes Will, Rafal E. Dunin-Borkowski, Janina Maultzsch, Julien Bachmann, and Erdmann Spiecker*

Cite This: *ACS Nano* 2025, 19, 25017−25027

Read Online

ACCESS | Metrics & More | Article Recommendations | Supporting Information

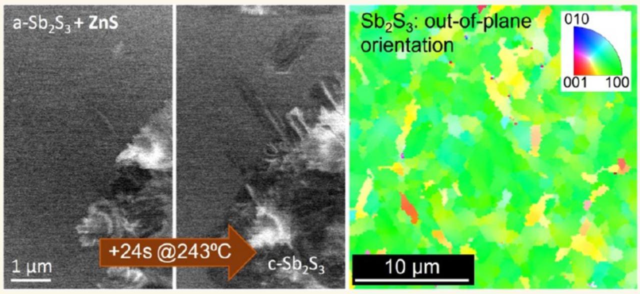

ABSTRACT: **Antimony sulfide (Sb_2S_3), a compound of earth-abundant elements with a highly anisotropic, quasi-layered crystal structure, has triggered growing interest as a solar absorber in photovoltaics and as a phase-change material in memory devices. However, challenges remain in achieving high-quality thin films with controlled nucleation and growth for optimal performance. Here, we investigate the phase transformation, crystal structure and properties, as well as the growth and degradation of atomic layer-deposited Sb_2S_3 thin films using *in situ* TEM and correlative *ex situ* analysis. The as-deposited amorphous films crystallized at 243 °C, forming grains with an [100] out-of-plane texture that developed into tens to hundreds of micrometer-long, leaf-shaped grains. Introducing an ultrathin ZnS interfacial layer increased nucleation density, resulting in few-micrometer-sized, more uniform grains while retaining the overall [100] texture. *In situ* observations and subsequent crystal orientation analysis with cutting-edge 4D-STEM and EBSD revealed that the grains grew faster along the [010] ribbon direction and that the bare films underwent early-stage degradation, forming holes in amorphous regions during annealing. The ZnS interlayer mitigated degradation, stabilizing the films and improving their uniformity. These findings offer valuable insights for optimizing Sb_2S_3 thin films for applications as both solar cell materials and phase-change materials.**

KEYWORDS: *Sb_2S_3, ALD, phase transition, correlative microscopy, in situ TEM*

INTRODUCTION

Antimony sulfide (Sb_2S_3) and related antimony chalcogenides have attracted considerable interest for optoelectronic and photovoltaic applications due to their favorable semiconductor properties, including a direct bandgap, high absorption coefficient, and chemical stability. These characteristics make Sb_2S_3 a promising material for solar cells,[1−23] photodetectors,[24−26] and thin-film transistors.[26] Recent studies[4,5,8,9,12,18−21,27] have demonstrated significant progress in antimony trichalcogenide photovoltaics and device integration, highlighting advances in film processing and interface engineering. Their power conversion efficiency has hit over 10%,[9,18,21,22] almost at the level required for industrial applications. The ability to process Sb_2S_3 into high-quality thin films is crucial for optimizing device performance, yet challenges remain in controlling its crystallization and film morphology.

Beyond optoelectronics, Sb_2S_3 is increasingly explored as a phase-change material (PCM) for nonvolatile memory and thermal switching devices.[28−34] Its rapid and reversible phase transformations between amorphous and crystalline phases, coupled with a significant contrast in electrical and optical properties, make it a potential alternative to conventional PCMs like the Ge−Sb−Te family.[35] Despite its promise, a fundamental understanding of the crystallization mechanisms of Sb_2S_3,

Received: March 12, 2025
Revised: June 17, 2025
Accepted: June 17, 2025
Published: July 4, 2025

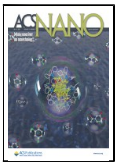

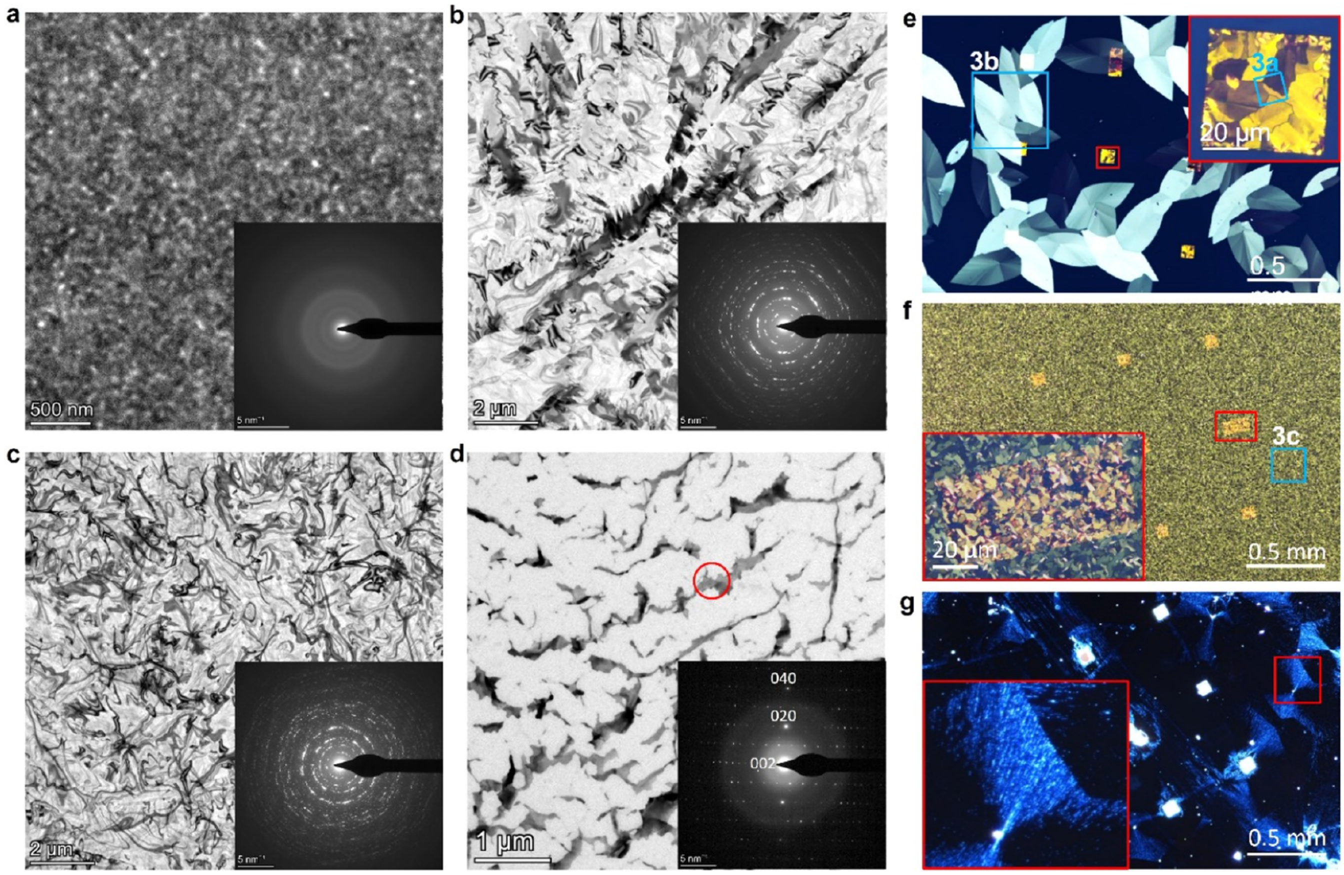

Figure 1. (a−d) bright-field (BF-) TEM images and selected area electron diffraction (SAED) patterns as insets of the antimony sulfide thin films at different deposition and annealing conditions. (a) The as-deposited a-Sb_2S_3 thin film. (b) The film in (a) after annealing at 250 °C for 10 min in TEM. (c) ZnS/a-Sb_2S_3 film after annealing at 250 °C for 10 min in TEM. (d) The a-Sb_2S_3 thin film from the same batch as (a) after annealing at 350 °C for 10 min in TEM. SA aperture for (a−c) included a large ∼13 μm diameter area of the thin films and only ∼460 nm diameter in (d), as marked by the red circled region. (e) Polarized light microscopy (PLM) of the sample shown in (b) supported on a Si/SiO_x TEM grid. The yellowish rectangles/squares (one magnified as an inset) are the 30 nm SiO_x membrane windows for TEM observations. (f) PLM of the sample shown in (c), with one membrane window magnified as an inset. (g) Dark-field optical micrograph of the sample shown in (d) revealing traces of evaporated Sb_2S_3. Blue boxed regions in parts (e) and (f) are further analyzed and shown in Figure 3.

including the role of structural anisotropy and interface effects, remains limited. A detailed insight into the mechanisms of nucleation, grain growth, and phase stability is critical for advancing its practical applications in both fields of optoelectronics and PCM.

A key aspect influencing device performance is the orientation of Sb_2S_3 crystals. These crystals crystallize in a highly anisotropic structure, forming covalently bonded quasi-one-dimensional ribbons. Charge transport is significantly more facile along the ribbon direction than in the perpendicular directions.[1,7,11,23,31] Therefore, controlling the crystal orientation in fundamentally anisotropic devices, such as solar cells, might provide an important avenue for performance optimization. If the ribbon orientation can be engineered to coincide with the desired carrier collection direction, losses can be minimized, potentially including losses caused by defects. Furthermore, maintaining precise control over the film morphology is equally important, as the spontaneous formation of elongated, needle-like structures along the ribbon direction, frequently observed in both microscopic and macroscopic crystals, can hinder the performance of semiconductor junction-based devices.

Atomic layer deposition (ALD) provides precise control over film thickness and composition, enabling the growth of highly uniform Sb_2S_3 thin films on arbitrary surfaces.[36,37] While ALD is primarily used for film growth in research and in the commercial production of high-added-value components, developments in ALD for the scalable, general-purpose production of thin films are on the horizon.[38] However, as-deposited Sb_2S_3 films are typically amorphous and require thermal annealing to crystallize into the desired crystalline phase. The crystallization process is influenced by factors, such as substrate properties, temperature, and the presence of interfacial layers, all of which affect the resulting texture, crystal size, and overall film quality. Despite significant progress, the underlying mechanisms governing nucleation, growth, and degradation during this transformation remain insufficiently understood.

This study combines *in situ* transmission electron microscopy (TEM) with correlative microscopy and spectroscopy to investigate the crystallization, grain growth, and degradation of ALD-deposited Sb_2S_3 thin films. We focus on elucidating how structural anisotropy, substrate curvature, and interfacial layers (specifically a ZnS adhesion layer) influence these processes. Using *in situ* TEM, we observe the amorphous-to-crystalline phase transition, track growth kinetics, and identify early-stage degradation phenomena. Complementary techniques, including 4D-STEM and Electron Backscatter Diffraction (EBSD), provide insights into the grain texture and orientation across different substrates. Furthermore, polarized light microscopy

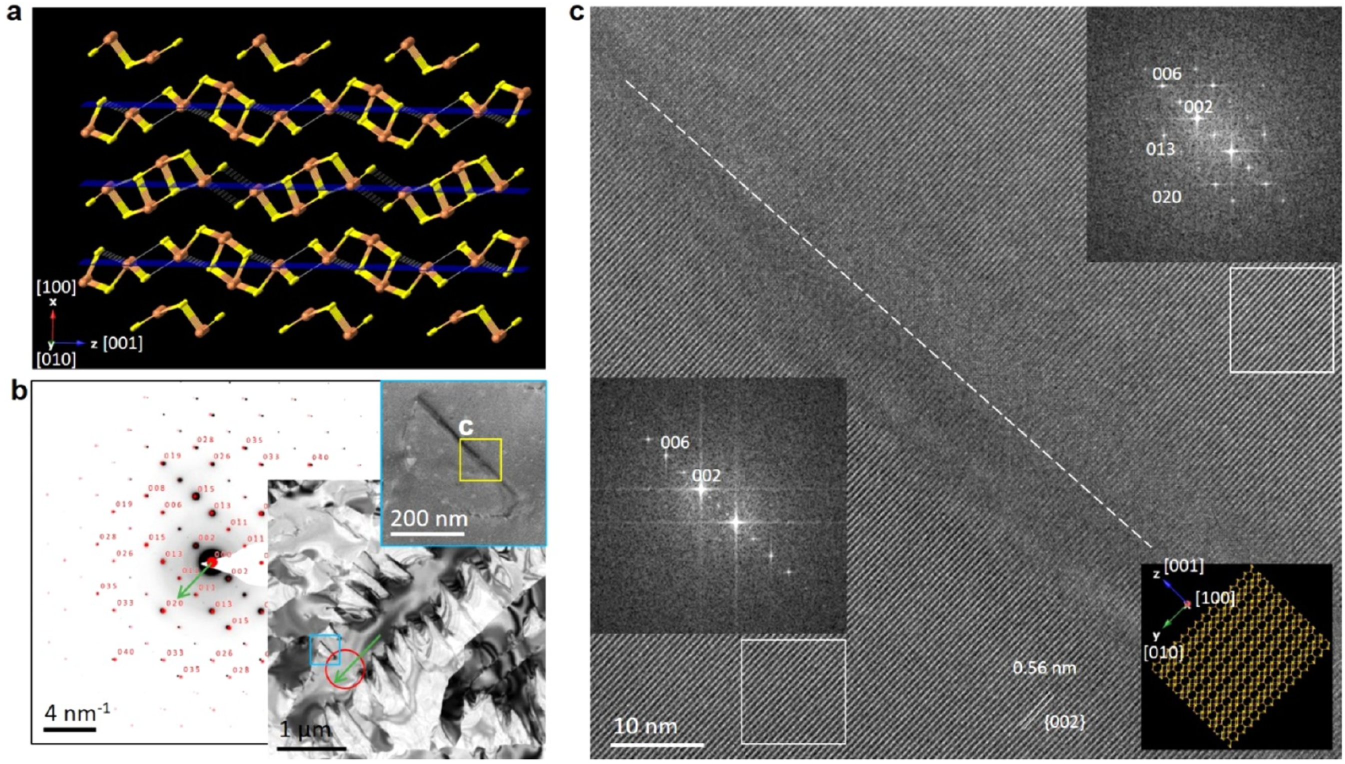

Figure 2. (a) Crystal structure of Sb_2S_3, (b) BF-TEM image highlights a long Sb_2S_3 crystal and the SAED from the red circled region with simulated pattern overlay, confirming the [100] Sb_2S_3 zone axis, and the grain growth direction along the [010] direction (green arrow). The blue boxed region is shown magnified as an inset. (c) HRTEM lattice image from the blue box region in (b), confirming the growth direction of [010] and the tangent direction of the bent film along the [001] direction.

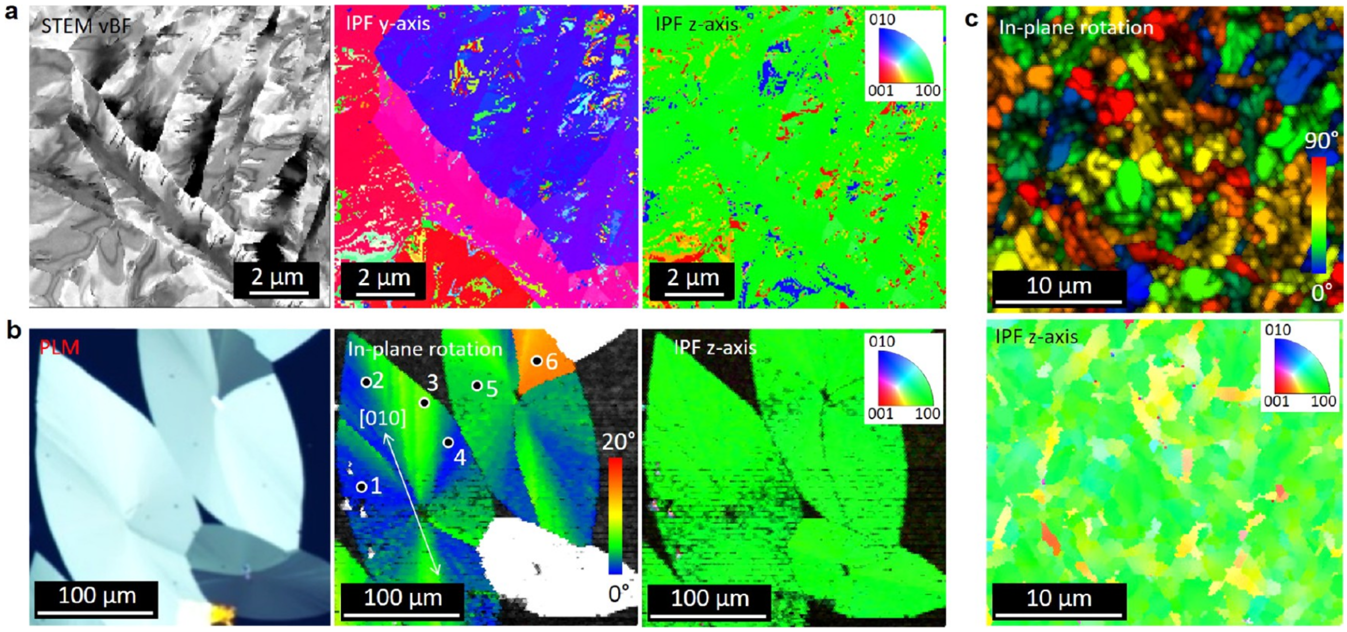

Figure 3. Crystal orientation analysis. (a) Crystal orientation maps (inverse pole figure, IPF) with the precession-assisted 4D-STEM dataset acquired in a thin window (blue box in the inset of Figure 1e. b,c Crystal orientation maps evaluated using EBSD of Sb_2S_3 crystallites on the Si/SiO_x substrate, as marked by the blue boxes in Figure 1e,f, respectively. The in-plane rotation maps in (b) and (c) are presented in a rainbow color scheme to best visualize the relative rotation angle of the [010] crystal direction in the large leaf-like grains. The black dots (and numbers) in the maps indicate where the Raman point measurements were carried out (shown in Figures 4 and S3). Further representation of the EBSD data in the normal IPF and PF is shown in Figure S5 for completeness.

and polarization-dependent Raman spectroscopy are applied in correlative terms with structural information derived from TEM/SEM to elucidate the orientation dependence of the vibrational modes.

https://doi.org/10.1021/acsnano.5c04342
ACS Nano 2025, 19, 25017−25027

RESULTS AND DISCUSSIONS

Phase Transformation of Sb_2S_3. Figure 1a−d illustrates the phase evolution of ALD-deposited antimony sulfide thin films, as observed by using bright-field TEM (BF-TEM) and selected area electron diffraction (SAED). The as-deposited films are amorphous (a-Sb_2S_3), as confirmed by the granular features in TEM imaging and the absence of sharp diffraction spots or rings in SAED (Figure 1a). The presence of an ultrathin ZnS interfacial layer does not significantly alter the morphology or diffraction pattern of the as-deposited films. Its presence is, however, confirmed through the Zn signals in EDX spectra (Figure S1), which are absent in the thin films without the ZnS layer.

After annealing above 243 °C in the vacuum of TEM, the amorphous thin films transform into the crystalline phase, both with and without the ZnS interfacial layer. The diffraction contrast TEM images reveal the crystal phase of Sb_2S_3 with strong bending contours (Figures 1b−d, 2d, and 3, further discussed later). This enables an easy differentiation of the crystal phase from the as-deposited amorphous phase due to the strong diffraction contrast, captured either using BF-TEM or complementary BF-, annular bright field (ABF-), and annular dark field (ADF-) STEM imaging modalities (cf. Figure S2 andvideos). Whereas, the high-angle annular dark-field (HAADF-) STEM images suppress the diffraction contrast and best reveal the crystal grain boundaries.

The amorphous-to-crystalline phase transformation temperature of Sb_2S_3 was carefully and consistently confirmed in five *in situ* annealing experiments (four experiments using a-Sb_2S_3 and one using ZnS/a-Sb_2S_3). In a first exploratory experiment, the temperature was increased by 50 °C in each step and held for at least 3 min to observe possible phase transformation. Here, the thin film crystallized after heating from 200 to 250 °C and holding at 250 °C. In a subsequent experiment, the temperature was first ramped to 200 °C and then increased by 5 °C per step. Here, the phase transformation could be narrowed down to take place between 240 and 245 °C. The corresponding video documenting the phase transformation is provided in Video S1, which is further analyzed in Figure 5 and discussed later below. Consequently, we carried out an additional experiment where the temperature was slowly ramped to 242 °C and held there for 30 min. During this period, no indication of a phase transformation was observed. Upon raising the temperature to 243 °C, crystalline grains evolved within 2 min. Repeating this protocol for a ZnS/a-Sb_2S_3 thin film yielded the same phase transformation temperature of 243 °C for a-Sb_2S_3 to Sb_2S_3 in vacuum. Thus, our systematic *in situ* investigations reveal that the phase transformation takes place reproducibly and independently of the interlayer at a defined temperature of 243 °C. The identified phase transformation temperature is in agreement with the range reported in the literature[29−31] but is much more precise.

Role of the ZnS Interlayer on Crystal Size. As described above, the ZnS interlayer plays a significant role in controlling the grain size. Without the interlayer, grain sizes of up to 10 μm in length and a few micrometers in lateral width are observed on the thin SiO_x windows for TEM observations (Figure 1b, inset in e). The Sb_2S_3 grains reach even hundreds of microns on flat surfaces of Si/SiO_x, which were not accessible by TEM, as revealed by polarized light microscopy (PLM, Figure 1e). This difference in size, dependent on the underlying surface curvature (buckled freestanding SiO_x membrane vs flat native SiO_x on Si), points to the influence of substrate topography on nucleation density. In contrast, the ZnS interlayer promotes a higher nucleation density, yielding smaller, more uniform grains of around 2−3 μm (Figure 1c,f), which is independent of the underlying substrate topology. The results suggest that ZnS provides heterogeneous nucleation sites, dictating grain size and minimizing the significant variability observed in ZnS-free samples. Thus, the interlayer also leads to a much higher degree of in-plane isotropy (further elaborated in Figure 3b,c and discussed therein) due to the finer grain structure as compared to the micrometer-sized leaf structure without ZnS.

Evaporation of the Sb_2S_3 Thin Films. Upon further heating an Sb_2S_3 sample to 350 °C, evaporation of the crystalline Sb_2S_3 film was observed, with grain boundaries initiating the degradation process (cf. frames 340−456 inVideo S2). The BF-TEM image and the corresponding indexed SAED pattern in Figure 1d and as the insets, highlight the preferred loss of material along the [010] direction. This is also indicated by the aligned traces of the residual film fragments in Figure 1g. All these suggest a potential path for sulfur volatilization at elevated temperatures in vacuum, consistent with previous findings on thermal instability in similar sulfide compounds.[31] In regions protected from vacuum exposure, such as the periphery of the TEM grid, the Sb_2S_3 film remained stable, illustrating the influence of environmental conditions on its stability. To elucidate the loss of sulfur, we performed EDXS analysis of a-Sb_2S_3/ZnS samples before and after annealing at 250 °C (Figure S7). The Sb:S atomic ratio remained close to 2:3, with only an ∼1 at. % variation, confirming minimal sulfur loss at the phase transformation temperature (and *in situ* TEM conditions). In contrast, the Sb_2S_3 samples annealed at 350 °C showed a ∼4 at. % reduction in sulfur content (compared to as-deposited), consistent with sulfur sublimation during high-temperature degradation of crystalline Sb_2S_3.

Texture of the Sb_2S_3Thin Films. Sb_2S_3 is a biaxial, highly anisotropic material that crystallizes into an orthorhombic structure belonging to the *Pnma* (#62) space group, with lattice parameters $a = 1.131$ nm, $b = 0.386$ nm, and $c = 1.123$ nm,[39] as shown in Figure 2a. The structure can be viewed as $[Sb_4S_6]_n$ ribbons extended with the strongest (shortest) covalent bonds along the [010] direction and weaker (longer) interactions along [100]. The weakest (longest) covalent bonds along [100] form a quasi-2D layered structure. This highly anisotropic nature of the crystal structure facilitates the anisotropic growth of the crystals. We note that, in other studies, Sb_2S_3 is assigned to the Pbnm (#62) space group, where the axes are permuted and thus the indices are referred to differently.

The Sb_2S_3 crystals grown on the SiO_x membrane windows mostly exhibit an elongated shape, which is best revealed by the HAADF-STEM images (cf. Figure S2) via their crystal grain boundaries. Strong bending contours are also visible, indicating high stress after thin-film crystallization. Furthermore, periodic folds, i.e., the short lines perpendicular to the grain boundary seemingly "carving" into the crystals along the long grain boundaries, can very often be seen (cf. Figures 1b, 2b, 5b, and S2). Although the bending contours complicate TEM analysis of grains, they provide valuable information about the character of the bending and folds in the thin films, given that the images were acquired under controlled diffraction conditions, which require defined sample tilt conditions, in either BF-TEM or ADF-STEM modality. Figure 2b highlights a long grain with periodic folds along the grain boundary. The SAED pattern taken from the red-circled region can be easily indexed to be very

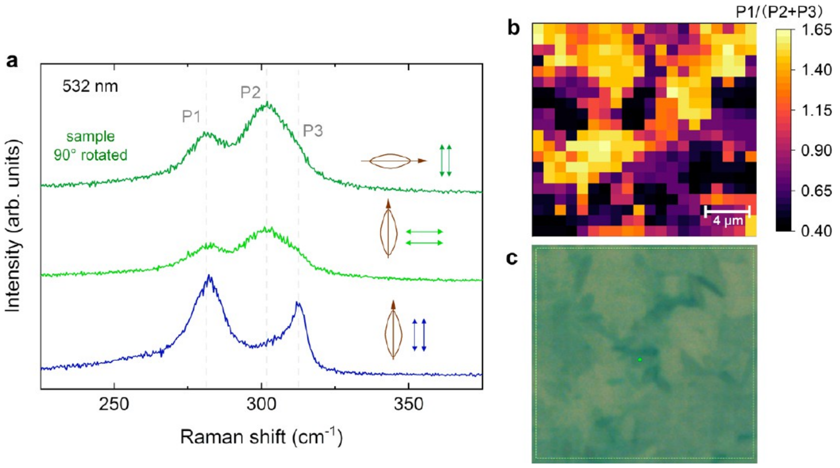

Figure 4. Raman spectroscopy analysis of the Sb_2S_3 samples. (a) Raman spectra of the Sb_2S_3 thin film with its [010] in-plane orientation parallel (blue line) and perpendicular (light green and dark green lines) to the laser and analyzed polarization. (b) Raman map of the ZnS/Sb_2S_3 film showing the amplitude ratio of the *P*1 peak (~282 cm^{-1}) and the sum of the *P*2 and *P*3 peaks (~301 cm^{-1} and ~312 cm^{-1}). (c) Optical microscope image of the area measured in the Raman map in (b).

close to the [100] zone axis. The diffraction vector and corresponding image confirm the long axis of the crystal was grown along the [0k0] direction, i.e., the ribbon direction, as indicated by the green arrows. Along the long axis at the center of this crystal, a more homogeneous contrast is revealed compared to that close to the folds, indicating that the crystals are flat in the middle and are bent/inclined closer to the folds.

The contrast at the periodic folds at the edge along the grain boundary is quite different. One of the folds, marked by the blue box in Figure 2b is magnified and shown as an inset on top. We further examined the region across the fold using HRTEM lattice imaging (in Figure 2c). The *{002}* lattice with 0.56 nm spacing is clearly revealed, whereas the *{002}* lattice could only be revealed on the top-right side via the fast Fourier transform (FFT, inset) pattern, whereas the lower-left region only preserved the *{00l}* system row of the lattice, as seen in the FFT, due to bending and tilting out of the zone axis. This indicates that the ribbons in the film across the folds bend and tilt inward or outward from the viewing direction, i.e., ***along*** the ribbon direction. This characteristic bending is likely a consequence of the crystal anisotropy, the growth kinetics, and stress relaxation mechanisms.

As expected for a quasi-2D layer structure of Sb_2S_3 and as locally indicated by the SAED pattern analysis, a highly [100]-textured structure is obtained. To confirm this, we performed crystal orientation analysis using precession-assisted nanobeam 4D-STEM on the Sb_2S_3 thin film supported on the SiO_x membrane (Figure 3a), large-area EBSD in the SEM (Figure 3b for Sb_2S_3 and Figure 3c for ZnS/Sb_2S_3) and polarization-dependent Raman spectroscopy (further detailed in Figure 4 and the text below) correlatively. In all cases, the inverse pole figures (IPF) along the *z*-axis (defined w.r.t. image coordinate, i.e., out-of-plane direction) confirm the dominance of a [100] out-of-plane texture. The in-plane maps, e.g., IPF along the image *y*-axis in Figure 3a, clearly reveal that the long crystal grains extend along the [010] direction, consistent with the local SAED and HRTEM results above. We note that the noise pattern (i.e., small clusters of blue and red pixels among the dominant green pixels in the IPF *z*-axis) in Figure 3a is due to strong bending of the film and failure of the orientation indexing routine at those locations, which is even more severe when analyzing the data without beam precession (cf. Figure S4). Nevertheless, the few grains indexed to be close to [201] and [301] (orange and yellow grains as rendered in Figure 3c IPF along the *z*-axis) in the ZnS/Sb_2S_3 sample are carefully validated to be sample characteristics. These grains can be mainly due to kinetically confined competition of grain growth and dictated by the epitaxy of Sb_2S_3 on the ZnS layer, which was found to be randomly oriented nanoparticles from our earlier work.[3] These high-index-oriented grains can create high carrier mobility channels in the out-of-plane direction, which is a desirable property for solar cell applications.[13]

The large leaf-like Sb_2S_3 crystallites grown on the Si/SiO_x surface also show [100] textures. All grains are dominantly [010] oriented along the long axis of the "leaves", only exhibiting an in-plane rotation of up to 8°, which is also clearly reflected in the PLM (cf. Figure 3b). We note that even though these grains share a [100] out-of-plane axis, they have slight rotations around the ribbon ([010]) direction. The in-plane rotation maps (Figure 3b) thus highlight these small misorientations: grains with only a few degrees of in-plane tilt appear in different colors. In other words, grains that coincide in the out-of-plane view can still produce distinct colors in the rotation map due to minor in-plane tilts or rotations. Such rotation likely results from the highly anisotropic mechanical properties of Sb_2S_3 and the anisotropic growth rate, which caused internal stress during growth. This is consistent with observations of the bending/tilting boundary and strong strain contrast (Figure 2b,c). The larger the grains, the more stress accumulation and the more likely they are to show such tilts or rotations. The smaller crystalline grains nucleated and grown on the ZnS interlayer also show a dominant [100] out-of-plane texture. However, a few grains appear to be [100] and [101] out-of-plane, which is likely due to the high density of nucleation and competitive crystal growth (further discussed later). Grazing incidence XRD of this sample also confirms the [100] out-of-plane texture over a mm scale (cf. Figure S5).

Raman Spectroscopy of the Sb_2S_3Thin Films. We performed polarization-dependent Raman spectroscopy on the same sample shown in Figure 3b at spots with known in-plane rotation (indicated by the numbers in Figure 3b) to correlatively probe the Raman response as a function of the known crystal orientation. Figure 4a shows the Raman spectra of a "0° position" (spot 1 in Figure 3b) with parallel polarization of

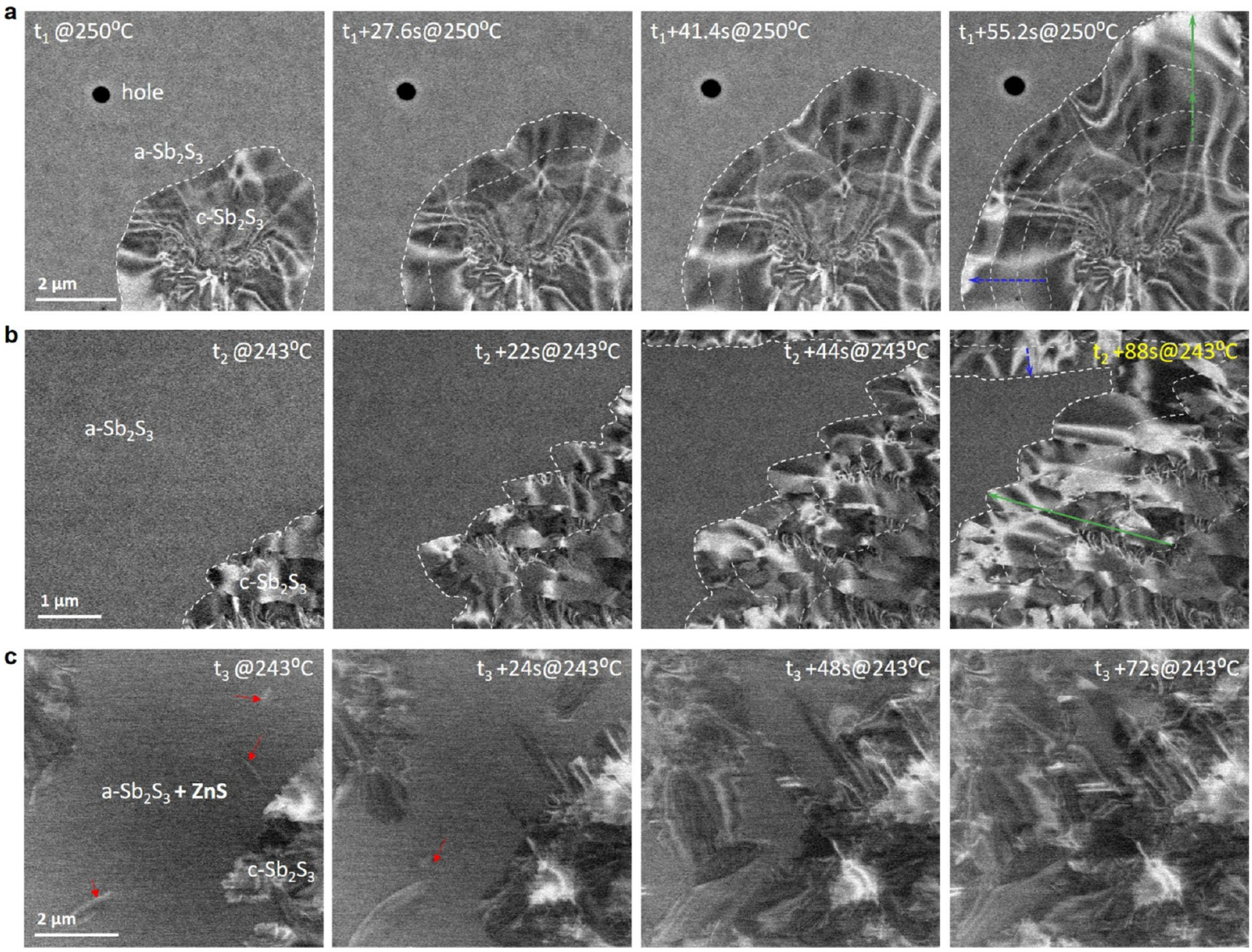

Figure 5. ***In situ*** **STEM observations of the nucleation of c-Sb2S3 and its growth from ALD a-Sb2S3 thin films (a, b) and from the ZnS/a-Sb2S3 film (c). (a) Snapshots extracted from experiment #1 (full movie in Supporting Information). Here, 2D isotropic growth of Sb2S3 at the initial nucleation site, as well as the formation and expansion of a hole in the a-Sb2S3 film, were observed. (b) Snapshots extracted from experiment #2 (full movie in Supporting Information). Growth of c-Sb2S3 far away from its initial nucleation site appeared as densely packed grains grown along a common crystallographic direction (further analyzed in Figure 3). (c) Snapshots extracted from experiment #3 (full movie in Supporting Information). At the same temperature as in exp. 2, a higher density of nucleation sites was observed. No holes were found in the entire TEM grid after the phase transformation was completed.**

incoming and detected light along the [010] in-plane direction (dark blue) and perpendicular to the [010] direction (middle and top green lines). The most dominant Sb_2S_3 Raman modes are the *P1* peak (282 cm^{-1}) and the *P2* and *P3* peaks (301 cm^{-1} and 312 cm^{-1}), marked by dashed lines. Depending on the orientation of the polarization, the intensity ratio of the *P1* to *(P2 + P3)* peaks changes: for polarization along the [010] direction (long axis of the leaf shape), the amplitude of the *P1* peak is higher than that of the *(P2/P3)* peaks, and vice versa for polarization perpendicular to the [010] axis. The same behavior is observed when the Sb_2S_3 sample is rotated by 90° instead of rotating the polarization of the laser and analyzer (dark green line in Figure 4a).

At locations with slightly different in-plane rotations [5° (green/spot 3 and 5) and 12° (orange/spot 6), as indicated in the in-plane orientation map (Figure 3b)], we observed small variations in the Raman spectra, specifically in the intensity ratio of the *P2* to *P3* peaks (Figure S3). As the in-plane rotation increases, the *P2* peak becomes more prominent, while the *P1* peak decreases, eventually leading to the combined *P2* + *P3* peak surpassing the intensity of the *P1* peak.

Based on the amplitude ratio between the *P1* and *(P2 + P3)* peaks, which indicates the crystalline orientation, we analyzed the ZnS/Sb_2S_3 film. Due to the highly [100] out-of-plane texture and varying [010] in-plane orientation of the smaller crystalline grains in this sample (see Figure 1f), strong polarization contrast was observed. We acquired a Raman map of 20 × 20 points over a field of view of $20 \times 20\ \mu m^2$ (cf. Figure 4b). Here, we plot the amplitude ratio of *P1* to the *(P2 + P3)* peaks. The polarization contrast in this map clearly reveals the crystal grains with different in-plane orientations, whereas their shape and size are in agreement with those revealed in Figure 1f. The different directions can be effectively distinguished from polarized Raman spectra.

In Situ **TEM Observations and Growth Kinetics of Sb_2S_3.** Having established the crystal grain morphology and orientation characteristics, we now come back to examine the growth kinetics, as observed in the *in situ* experiments. Figure 5 summarizes some key frames of the *in situ* ADF-STEM

https://doi.org/10.1021/acsnano.5c04342

observations. The full videos and simultaneously acquired BF-, ABF-, and HAADF-STEM images are provided as Supporting Information. Since the amorphous-to-crystalline phase transformation is irreversible, and the field of view, observation frame rate, and resolution (sampling size) are dependent on each other, it is a matter of luck to capture the initial nucleation at high spatial and temporal resolution, which can be even more challenging when the nucleation density is low

Figure 5a highlights the growth front of a crystal grain from a nucleation site in the a-Sb_2S_3 thin film (without a ZnS interlayer) at 250 °C. It appears that the initial growth is isotropic in all directions, with a growth rate of ~40 nm/s. Despite the strong bending contours, no clear indication of grain boundaries (e.g., abruptly broken bending contours) can be identified, suggesting that the grain is still single crystalline. After about 30 s, the growth along the upward direction (in the image coordinate, indicated by the green arrow) became faster, with a growth rate of almost 100 nm/s. With the knowledge obtained from *ex situ* ACOM analysis, it is reasonable to assume that the faster growth direction is along [010]. Assuming a constant growth rate hereafter and no coalescence, this would lead to oval-shaped crystals with an aspect ratio of about 2.5, which is in good agreement with the observed large "leaves" on the surface of the planar Si/SiO_x substrate. Furthermore, a hole in the a-Sb_2S_3 region is observed. The diameter of the hole grew slightly at a much slower speed compared to the crystallization front. The image intensity at the rim of the hole is slightly higher, indicating piled-up materials (based on the ADF-STEM image contrast mechanism). This evidence shows that the holes formed in the amorphous region are a consequence of the early stage of dewetting rather than sublimation, which is different from the degradation of the crystalline film at higher temperatures discussed earlier. Figure 5b showcases the growth front of crystal grains within the a-Sb_2S_3 thin film (without a ZnS interlayer) at a slightly lower temperature of 243 °C. The morphology of the grains mimics those characterized in Figure 2d; thus, it is reasonable to assume that the major growth direction (from right to left) is along [010]. Despite being only a few degrees Celsius lower in temperature, this growth front extends at a much slower rate of about 35 nm/s compared to the previous observations (up to 100 nm/s). From about t_2 + 40 s, another grain emerged from the top side of the frame with a growth rate of about 10 nm/s.

In the presence of an ultrathin (1 nm) ZnS interlayer between the oxidic substrate and the antimony sulfide film, a much higher density of Sb_2S_3 nuclei is observed in the a-Sb_2S_3, as shown in Figure 5c (red arrows) and Video S3. Due to the higher density, grain growth is stopped by impinging neighboring grains before the typical leaf-shaped growth characteristics evolve, resulting in a much finer grain structure compared to the thin films without the interlayer. Thus, the analysis of the growth kinetics reveals that the leaf-shaped morphology stems from the anisotropic growth kinetics of Sb_2S_3, and here the growth is fastest in the [010] direction. In addition to this, the growth kinetics are highly temperature-dependent leading to a significantly slower growth rate when reducing the crystallization temperature from 250 ° C to 243 ° C. We would expect that with longer annealing time above the crystallization temperature, grains may grow larger until the entire film transforms to crystalline, and Ostwald ripening may occur. At higher temperatures, sublimation and degradation of the film will eventually take place.

Role of the ZnS Interlayer on Thin-Film Degradation. During *in situ* annealing around 250 °C, holes in the yet-to-transform a-Sb_2S_3 layer were observed in thin films without the ZnS interlayer (Figure 5a and Video S1), which is attributed to the very early stage of film degradation via solid-state dewetting,[40] as evidenced and discussed above. With longer annealing times at a constant temperature of around 250 °C, these holes further expand. In the thin films with a ZnS interlayer, no such holes were observed under identical conditions. It is interesting to note that the overall phase transformation kinetics with and without ZnS are rather similar. The higher density of nuclei with ZnS is, in part, countered by the fast anisotropic growth along the [010] direction in the thin film without ZnS (cf Figure 5a,b). Thus, we do not expect to kinetically suppress the thin film degradation/dewetting in the amorphous film; consequently, the observed higher stability of the film on the ZnS interlayer can be attributed to a lowered interface energy between the a-Sb_2S_3 film and ZnS as compared to SiO_x. These observations document that the role of the interlayer is 2-fold: (i) ZnS provides heterogeneous nucleation sites, leading to a finer and more isotropic microstructure after crystallization, and (ii) ZnS acts as an adhesion layer, lowering the interface energy toward the substrate. However, it does not lower the phase transformation temperature or the growth kinetics of Sb_2S_3 crystal growth. We note that all our observations were made under high vacuum (TEM conditions), whereas device processing often occurs in inert or sulfur-containing atmospheres. The high vacuum could promote sulfur evaporation and enhance dewetting. In addition, electron-beam exposure was kept at a low dose to minimize any beam-induced crystallization or damage. However, the observing electron beam can induce carbon contamination (electron-beam-induced deposition, EBID), particularly at high magnifications, i.e., high-dose conditions. This alters the kinetics of crystallization (cf. frames 1260−1360 in Video S1, where the growth front was hindered and new nucleation sites were observed) and evaporation. We observed that the extensively observed regions at lower temperatures of 250 °C, which were carbon-contaminated, were better protected against evaporation at the higher temperature of 350 °C (cf. frames 1456−1501 in Video S2). Our observations suggest that while vacuum and beam effects cannot be entirely ruled out, they are unlikely to qualitatively alter the observed behavior of phase transformation and hole formation in the amorphous layer near the crystallization temperature. However, as the evaporation of the crystalline thin film is associated with the loss of materials, in particular sulfur (as discussed above, cf. Figure S7), the *in situ* TEM conditions in vacuum may have lowered the critical temperature of evaporation compared to processing conditions in inert or sulfur-containing atmospheres.

The ZnS interlayer used in this study is ultrathin (~1 nm) to meet both structural and functional objectives. For nucleation control and orientation alignment, it is the topmost interfacial atomic layers that are deterministic, not the total film thickness. Similar effects have been observed using CdS interlayers, where local epitaxy and favorable bonding promote vertically oriented $Sb_2(S,Se)_3$ films. By using different interlayers, the lattice mismatch and interfacial chemistry between the sulfide buffers and Sb_2S_3 can tune these effects, but the thickness beyond a few monolayers plays a secondary role. From a device perspective, a thicker ZnS layer can hinder carrier transport. In our previous studies of functional solar cell performance, we have found ~1 nm ZnS to be optimal in solar cells, with thicker layers impairing efficiency.[3] Thus, our ZnS interlayer thickness was selected to optimize both crystallization behavior and device-relevant functionality.

CONCLUSION

This study provides a comprehensive understanding of the phase transformation, crystal growth, and degradation mechanisms of ALD-deposited Sb_2S_3 thin films. Using *in situ* TEM, we determined that the crystallization of amorphous Sb_2S_3 films occurred at 243 °C with anisotropic crystal growth, driven by its intrinsic structural anisotropy. Correlative microscopy and spectroscopy analyses confirmed the [100] out-of-plane texture and the orientation-dependent Raman signals. The introduction of an ultrathin ZnS interfacial layer significantly enhanced nucleation density, leading to smaller, more uniform grains while mitigating early-stage degradation. Conversely, ZnS-free films exhibited larger, leaf-shaped grains with hole formation and early-stage degradation before phase transformation. Evaporation of the film took place at a higher temperature of 350 °C under vacuum, initiated along grain boundaries, and proceeded preferentially along the [010] ribbon direction.

These findings highlight the critical roles of interfacial engineering and substrate properties in controlling crystallization dynamics and improving film stability. The combined use of *in situ* TEM, 4D-STEM, EBSD, and correlative optical spectroscopy provides a robust framework for unraveling complex growth phenomena, and bridging structural, chemical, and optical insights. By addressing the challenges of controlling nucleation, grain growth, and phase stability, this work establishes guidelines for tailoring Sb_2S_3 thin films and offers valuable insights into their optimization in both optoelectronic and phase-change applications. The crystallization and growth phenomena we observe are expected to apply to Sb_2S_3 films produced by other deposition methods (e.g., chemical vapor deposition or sputtering). Our findings should have broad applicability across different film growth approaches.

MATERIALS AND METHODS

Atomic Layer Deposition. ZnS and Sb_2S_3 were deposited using a homemade hot-wall atomic layer deposition (ALD) reactor onto Si/SiO_x TEM grids with SiO_x windows, following established protocols.[2,3] The precursors used were diethylzinc (DEZ, 95%, abcr), tris(dimethylamido)antimony(III) ($Sb(NMe_2)_3$, 99.99%, Sigma-Aldrich), and H_2S (3% vol in N_2, Air Liquide). Nitrogen was used as the carrier gas, and the reaction temperatures were 150 and 120 °C for the deposition of ZnS and Sb_2S_3, respectively. The precursors were kept at room temperature, and the opening, exposure, and pumping times were 0.2, 15, and 15 s in all cases, except for the Sb precursor, which was opened for 1.5 s and kept at 40 °C due to its lower vapor pressure. In our experiments, 600 ALD cycles were used to deposit Sb_2S_3 (yielding ~36 nm film thickness on flat substrates as measured by ellipsometry), and 16 cycles were used for the ZnS interlayer (~1 nm thickness)

We note that ALD deposited a-Sb_2S_3 on both sides of the Si/SiO_x TEM grid. In most of the SiOx windows, we observed overlapping Sb_2S_3 crystal films on both sides of the SiO_x membrane (e.g., Figure 1c). This overlap can be identified by the continuous bending contour (of the crystal on one side), which seemingly crosses the grain boundaries (of the crystals on the other side). Luckily, in the center and lower-right window of a TEM grid shown in Figure 1e, only the a-Sb_2S_3 on one side of the SiO_x membrane has transformed into Sb_2S_3 crystal (inset in Figure 1e), while the other side remained amorphous. This structure made it more straightforward to analyze the crystal orientation of the crystals with 4D-STEM. In future experiments, we plan to prevent double-sided coating (for example, by masking the backside of the grids) to avoid this issue. However, as noted above, this minor issue does not affect our analysis since we restricted measurements to regions where only a single-side film has transformed.

Light Microscopy. Polarized light microscopy (PLM) was carried out using a Nikon Eclipse LV100ND microscope with a linear polarizer (L-Pol) in the condenser and an analyzer before the detector. During the experiment, the polarizer was rotated until the minimum reflection intensity from the known amorphous region was reached. This indicates that the L-Pol and analyzer are perpendicular to each other. Afterward, the samples were rotated until the strongest optical contrast was revealed. Images were acquired using the Nikon R2i color camera with auto white balance.

***In Situ* Observations in the TEM.** TEM experiments were performed either on a double Cs-corrected Thermo Fisher Scientific (TFS) Titan Themis platform operated at 300 kV or on a probe-corrected TFS Spectra 200 instrument. Since most imaging conditions involve undersampled nanoscale resolution (sampling), aberration correction was not critical. The HRTEM image shown in Figure 2 was acquired with the image corrector (of the Titan Themis TEM) carefully tuned to deliver a point resolution of 1 Å.

In situ observations were made in STEM mode with a probe convergence angle (α) of 21 mrad (on the spectra) and 15.7 mrad (on the Titan) and four imaging modalities—BF-, ABF-, ADF- and HAADF-STEM—simultaneously recorded. The detector collection angles were set so that the BF detector received up to $\alpha/2$, ABF covered from $\alpha/2$ to slightly > α, ADF from slightly > α to ~55 mrad, and HAADF received from ~56 mrad to ~200 mrad. In such way, the strong diffraction contrast and bending contours can be best visualized in ABF- and ADF-STEM images even at high speed and with noisy data sets, while the HAADF-STEM images can be used to identify grain boundaries, voids, and holes.

A Gatan furnace heating holder system, model 652, is used to perform the *in situ* annealing experiments. The temperature accuracy in the steady state (e.g., during holding) was verified by quantitatively evaluating the dewetting phenomena of identical metal thin films compared to a carefully calibrated MEMS chip-based heating holder, and the results show good agreement.[41] The Si/SiO_x membrane window grids were mounted so that the windows were aligned at the center of the heating furnace. The temperature was manually controlled by the controller knob. The homogeneous size of crystals found on the surface of the TEM grid after annealing experiments indicates no critical temperature gradient during the experiments.

Crystal Orientation Mapping. Precession-assisted nanobeam 4D-STEM experiments were performed using a TESCAN Tensor instrument operated at 120 kV. This instrument is equipped with a Dectris Quadro hybrid pixel detector and a precession unit capable of running up to 72 kHz. We applied a focused probe with a 2 mrad convergence angle and a 250 pA probe current. Further acquisition parameters were: 1° precession angle, 1 ms dwell time, and 200 × 200 scanning points. Indexing and IPF were evaluated using TESCAN software with the crystal structure of Sb_2S_3. Beam precession greatly improved the indexing success rate and generated orientation maps with a higher confidence level (cf. Figure S4 results with and without beam precession).

EBSD measurements were carried out on a Zeiss Gemini 560 equipped with an EDAX Clarity Super EBSD detector (AMETEK Inc., USA). The measurements were executed at 10 kV, with the probe current set to 150−250 pA and a pixel size of 2 μm for the Sb_2S_3 and 0.2 μm for Sb_2S_3/ZnS. After data collection, the EBSD maps were refined via spherical indexing[42] in OIM Matrix (AMETEK) with a precalculated master pattern using EMsoft.[43] The master pattern from EMsoft greatly improves the indexing quality compared to the native master pattern from the OIM Matrix.

Raman Spectroscopy. Raman spectroscopy of the Sb_2S_3 and Sb_2S_3/ZnS samples was performed using a HORIBA LabRam HR Evolution spectrometer with a laser wavelength of λ = 532.17 nm (2.33 eV), laser focus <1 μm, and an 1800 lines/mm grating. To avoid heating effects, laser powers below 0.5 mW were used. For the polarization-dependent measurements, a polarizer and an analyzer were integrated into the beam path to control the polarization of the laser and the passing direction of the scattered light. For the Raman map of the

Sb_2S_3/ZnS sample, a step size of 1 μm was used. All Raman spectra were calibrated by neon lines.

ASSOCIATED CONTENT

Data Availability Statement

The precession-assisted 4D-STEM datasets and the *in situ* observations are available in a public data repository with the accession DOI: 10.5281/zenodo.15536234

Supporting Information

The Supporting Information is available free of charge at https://pubs.acs.org/doi/10.1021/acsnano.5c04342.

Additional experimental results, including EDX spectra (Figures S1 and S7), STEM images (Figure S2), Raman data analysis (Figure S3), 4D-STEM data analysis (Figure S4), additional EBSD data visualization (Figure S5), and XRD data (Figure S6) (PDF)

Upon further heating an Sb_2S_3 sample to 350 °C, evaporation of the crystalline Sb_2S_3 film was observed, with grain boundaries initiating the degradation process (cf. frames 340-456) (Video S1)

In the presence of an ultrathin (1 nm) ZnS interlayer between the oxidic substrate and the antimony sulfide film, a much higher density of Sb_2S_3 nuclei is observed in the a-Sb_2S_3 (Video S2)

The phase transformation (Video S3)

AUTHOR INFORMATION

Corresponding Authors

Mingjian Wu − *Institute of Micro- and Nanostructure Research & Center for Nanoanalysis and Electron Microscopy (CENEM), Friedrich-Alexander-Universität Erlangen-Nürnberg, IZNF, Erlangen 91058, Germany;* orcid.org/0000-0003-2113-0245; Email: mingjian.wu@fau.de

Erdmann Spiecker − *Institute of Micro- and Nanostructure Research & Center for Nanoanalysis and Electron Microscopy (CENEM), Friedrich-Alexander-Universität Erlangen-Nürnberg, IZNF, Erlangen 91058, Germany;* orcid.org/0000-0002-2723-5227; Email: erdmann.spiecker@fau.de

Authors

Maïssa K. S. Barr − *Chemistry of Thin Film Materials, Materials Chemistry Section, Department Chemistry and Pharmacy, Friedrich-Alexander-Universität Erlangen-Nürnberg, IZNF, Erlangen 91058, Germany*

Vanessa M. Koch − *Chemistry of Thin Film Materials, Materials Chemistry Section, Department Chemistry and Pharmacy, Friedrich-Alexander-Universität Erlangen-Nürnberg, IZNF, Erlangen 91058, Germany;* orcid.org/0000-0003-4560-787X

Martin Dierner − *Institute of Micro- and Nanostructure Research & Center for Nanoanalysis and Electron Microscopy (CENEM), Friedrich-Alexander-Universität Erlangen-Nürnberg, IZNF, Erlangen 91058, Germany;* orcid.org/0000-0001-7386-5265

Tobias Dierke − *Chair of Experimental Physics, Department of Physics, Friedrich-Alexander-Universität Erlangen-Nürnberg, Erlangen 91058, Germany;* orcid.org/0000-0003-0002-5171

Penghan Lu − *Ernst Ruska-Centre for Microscopy and Spectroscopy with Electrons, Research Centre Jülich, Jülich 52425, Germany*

Pei-Chun Liao − *Chemistry of Thin Film Materials, Materials Chemistry Section, Department Chemistry and Pharmacy, Friedrich-Alexander-Universität Erlangen-Nürnberg, IZNF, Erlangen 91058, Germany*

Johannes Will − *Institute of Micro- and Nanostructure Research & Center for Nanoanalysis and Electron Microscopy (CENEM), Friedrich-Alexander-Universität Erlangen-Nürnberg, IZNF, Erlangen 91058, Germany;* orcid.org/0000-0003-0326-9913

Rafal E. Dunin-Borkowski − *Ernst Ruska-Centre for Microscopy and Spectroscopy with Electrons, Research Centre Jülich, Jülich 52425, Germany;* orcid.org/0000-0001-8082-0647

Janina Maultzsch − *Chair of Experimental Physics, Department of Physics, Friedrich-Alexander-Universität Erlangen-Nürnberg, Erlangen 91058, Germany*

Julien Bachmann − *Chemistry of Thin Film Materials, Materials Chemistry Section, Department Chemistry and Pharmacy, Friedrich-Alexander-Universität Erlangen-Nürnberg, IZNF, Erlangen 91058, Germany;* orcid.org/0000-0001-6480-6212

Complete contact information is available at: https://pubs.acs.org/10.1021/acsnano.5c04342

Author Contributions

M.W., J.W., J.B., and E.S. conceptualized the study and designed the experiments. M.W. performed the *in situ* TEM experiments, formal analysis and investigation, validated the study, wrote the original draft, wrote, reviewed, and edited the final draft. M.K.S.B. and V.M.K. performed the ALD sample preparation. M.D. performed the SEM-EBSD data acquisition and formal analysis. T.D. and J.M. performed the Raman measurements and formal analysis. P.L. coordinated and performed the precession-assisted 4D-STEM experiments and formal analysis. P.C-.L. performed the XRD measurements and formal analysis. R.E.D.B. established instrumentation for precession-assisted 4D-STEM and reviewed and edited the original draft. J.M., J.B., and E.S. acquired funding and reviewed and edited the original draft. All authors approved the final draft.

Notes

The authors declare no competing financial interest.

ACKNOWLEDGMENTS

We acknowledge funding from the Deutsche Forschungsgemeinschaft (DFG) via the research training school GRK 1896: "In-Situ Microscopy with Electrons, X-rays and Scanning Probes", and the Cluster of Excellence EXC 315 "Engineering of Advanced Materials". M.K.S.B., V.M.K. and J.B. acknowledge funding by the Bavarian-Czech Academic Alliance (BTHA) in the project "BaCzALD− Bavarian-Czech Alliance for Photo-active Films by Solution Atomic Layer Deposition" (grant number BTHA-JC-2024-2). T.D. and J.M. acknowledge support by the Deutsche Forschungsgemeinschaft (DFG, German Research Foundation), project number 447264071 (INST 90/1183-1 FUGG).

REFERENCES

(1) Barthwal, S.; Kumar, R.; Pathak, S. Present Status and Future Perspective of Antimony Chalcogenide (Sb_2X_3) Photovoltaics. *Acs Appl. Energy Mater.* **2022**, *5* (6), 6545−6585.

(2) Büttner, P.; Scheler, F.; Döhler, D.; Barr, M. K. S.; Bosch, M.; Rey, M.; Yokosawa, T.; Hinz, S.; Maultzsch, J.; Spiecker, E.; et al. Continuous, crystalline Sb_2S_3 ultrathin light absorber coatings in solar

cells based on photonic concentric p-i-n heterojunctions. *Nano Energy* **2022**, *103*, 107820.

(3) Büttner, P.; Scheler, F.; Pointer, C.; Döhler, D.; Yokosawa, T.; Spiecker, E.; Boix, P. P.; Young, E. R.; Mínguez-Bacho, I.; Bachmann, J. ZnS Ultrathin Interfacial Layers for Optimizing Carrier Management in Sb_2S_3-based Photovoltaics. *ACS Appl. Mater. Interfaces* **2021**, *13* (10), 11861−11868.

(4) Chen, G.; Luo, Y.; Abbas, M.; Ishaq, M.; Zheng, Z.; Chen, S.; Su, Z.; Zhang, X.; Fan, P.; Liang, G. Suppressing Buried Interface Nonradiative Recombination Losses Toward High-Efficiency Antimony Triselenide Solar Cells. *Adv. Mater.* **2024**, *36* (5), No. e2308522.

(5) Chen, G. J.; Zhao, J.; Chen, S.; Zheng, Z. H.; Su, Z. H.; Luo, J. T.; Liang, G. X. Perspective of environmentally friendly antimony selenide-based solar cell. *Appl. Phys. Lett.* **2024**, *125* (20), 200502.

(6) Chen, J.; Qi, J.; Liu, R.; Zhu, X.; Wan, Z.; Zhao, Q.; Tao, S.; Dong, C.; Ashebir, G. Y.; Chen, W.; et al. Preferentially oriented large antimony trisulfide single-crystalline cuboids grown on polycrystalline titania film for solar cells. *Commun. Chem.* **2019**, *2*, 121.

(7) Chen, J.; Li, G.; Xu, Z.; Xu, C.; Naveed, F.; Liu, B.; Zhang, Y.; Zhou, R.; Chen, C.; Wang, M.; et al. Recent Advances and Prospects of Solution-Processed Efficient Sb_2S_3 Solar Cells. *Adv. Funct. Mater.* **2024**, *34* (18), 2313676.

(8) Chen, S.; Ye, Y.-A.; Ishaq, M.; Ren, D.-L.; Luo, P.; Wu, K.-W.; Zeng, Y.-J.; Zheng, Z.-H.; Su, Z.-H.; Liang, G.-X. Simultaneous Band Alignment Modulation and Carrier Dynamics Optimization Enable Highest Efficiency in Cd-Free Sb_2Se_3 Solar Cells. *Adv. Funct. Mater.* **2024**, *34* (40), 2403934.

(9) Duan, Z.; Liang, X.; Feng, Y.; Ma, H.; Liang, B.; Wang, Y.; Luo, S.; Wang, S.; Schropp, R. E. I.; Mai, Y.; et al. Sb_2Se_3 Thin-Film Solar Cells Exceeding 10% Power Conversion Efficiency Enabled by Injection Vapor Deposition Technology. *Adv. Mater.* **2022**, *34* (30), 2202969.

(10) Farhana, M. A.; Manjceevan, A.; Bandara, J. Recent advances and new research trends in Sb_2S_3 thin film based solar cells. *J. Sci.:Adv. Mater. Devices* **2023**, *8* (1), 100533.

(11) Farhana, M. A.; Manjceevan, A.; Tan, H.-Y.; Yan, C.-F.; Bandara, J. A review on the device efficiency limiting factors in Sb_2S_3-based solar cells and potential solutions to optimize the efficiency. *Opt. Quant. Electron.* **2023**, *55* (8), 678.

(12) Fu, B.; Xiong, J.; Jv, T.; Chen, S.; Liang, T.; Ma, H.; Zhang, X.; Pan, D.; Zou, B.; Liang, G.; et al. Reaction Kinetics Regulation Suppressed Carrier Recombination Loss for High-Efficient Solution-Based Antimony Selenosulfide Photovoltaic Devices. *Adv. Energy Mater.* **2025**, 2500586.

(13) Jin, X.; Fang, Y.; Salim, T.; Feng, M.; Yuan, Z.; Hadke, S.; Sum, T. C.; Wong, L. H. Controllable Solution-Phase Epitaxial Growth of Q1D $Sb_2(S,Se)_3$/CdS Heterojunction Solar Cell with 9.2% Efficiency. *Adv. Mater.* **2021**, *33* (44), No. e2104346.

(14) Kim, D.-H.; Lee, S.-J.; Park, M. S.; Kang, J.-K.; Heo, J. H.; Im, S. H.; Sung, S.-J. Highly reproducible planar Sb_2S_3-sensitized solar cells based on atomic layer deposition. *Nanoscale* **2014**, *6* (23), 14549−14554.

(15) Kondrotas, R.; Chen, C.; Tang, J. Sb_2S_3 Solar Cells. *Joule* **2018**, *2* (5), 857−878.

(16) Pareek, A.; Katerski, A.; Kriisa, M.; Spalatu, N.; Krunks, M.; Acik, I. O. Towards all inorganic antimony sulphide semitransparent solar cells. *Sci. Rep.* **2025**, *15* (1), 1468.

(17) Pointer, C.; Büttner, P.; Scheler, F.; Döhler, D.; Mínguez-Bacho, I.; Bachmann, J.; Young, E. R. Elucidating Mechanistic Details of Photo-Induced Charge Transfer in Antimony Sulfide-Based p-i-n Junctions. *J. Phys. Chem. C* **2021**, *125* (33), 18429−18437.

(18) Ren, D.; Fu, B.; Xiong, J.; Wang, Y.; Zhu, B.; Chen, S.; Li, Z.; Ma, H.; Zhang, X.; Pan, D.; et al. PO_4^{3-} Tetrahedron Assisted Chelate Engineering for 10.67%-Efficient Antimony Selenosulfide Solar Cells. *Adv. Mater.* **2025**, *37* (8), No. e2416885.

(19) Ren, D.; Li, C.; Xiong, J.; Liang, W.; Cathelinaud, M.; Zhang, X.; Chen, S.; Li, Z.; Pan, D.; Liang, G.; et al. Heterogeneous Nucleation Regulation Amends Unfavorable Crystallization Orientation and Defect Features of Antimony Selenosulfide Film for High-Efficient Planar Solar Cells. *Angew. Chem. Int. Ed.* **2025**, *64* (1), No. e202413108.

(20) Tang, R.; Chen, S.; Zheng, Z.-H.; Su, Z.-H.; Luo, J.-T.; Fan, P.; Zhang, X.-H.; Tang, J.; Liang, G.-X. Heterojunction Annealing Enabling Record Open-Circuit Voltage in Antimony Triselenide Solar Cells. *Adv. Mater.* **2022**, *34* (14), No. e2109078.

(21) Tang, R.; Wang, X.; Lian, W.; Huang, J.; Wei, Q.; Huang, M.; Yin, Y.; Jiang, C.; Yang, S.; Xing, G.; et al. Hydrothermal deposition of antimony selenosulfide thin films enables solar cells with 10% efficiency. *Nat. Energy* **2020**, *5* (8), 587−595.

(22) Zhao, Y.; Wang, S.; Li, C.; Che, B.; Chen, X.; Chen, H.; Tang, R.; Wang, X.; Chen, G.; Wang, T.; et al. Regulating deposition kinetics via a novel additive-assisted chemical bath deposition technology enables fabrication of 10.57%-efficiency Sb_2Se_3 solar cells. *Energy Environ. Sci.* **2022**, *15* (12), 5118−5128.

(23) Zhao, Y.; Chen, X.; Li, J.; Xiao, X. A Review of Carrier Transport in High-Efficiency $Sb_2(S,Se)_3$ Solar Cells. *Sol. RRL* **2023**, *7* (23), 2300565.

(24) Lian, X.; Luo, L.; Dong, M.; Miao, Z.; Qi, X.; Cai, Z.; Wang, L. A review on the recent progress on photodetectors. *J. Mater. Sci.* **2024**, *59* (47), 21581−21604.

(25) Shen, Y.-C.; Lee, C.-Y.; Wang, H.-H.; Kao, M.-H.; Hou, P.-C.; Chen, Y.-Y.; Huang, W.-H.; Shen, C.-H.; Chueh, Y.-L. Embedded Integration of Sb2Se3 Film by Low-Temperature Plasma-Assisted Chemical Vapor Reaction with Polycrystalline Si Transistor for High-Performance Flexible Visible-to-Near-Infrared Photodetector. *ACS Nano* **2023**, *17*, 2019−2028.

(26) Deng, H.; Kang, Y.; Jia, Y.; Chen, Z.; Wang, W.; Xia, Y.; Lai, Y.; Cheng, S. Gate-controlled Sb_2S_3 thin film photodetectors for logic switches. *Opt. Lett.* **2023**, *48* (20), 5265−5268.

(27) Chen, S.; Chen, Y.; Aziz, H. S.; Zhang, H.-H.; Li, Z.-L.; Chen, Y.-X.; Zeng, Y.-J.; Zheng, Z.-H.; Hu, J.-G.; Su, Z.-H.; et al. A Cd-Free Electron Transport Layer Simultaneously Enhances Charge Carrier Separation and Transfer in Sb_2Se_3 Photocathodes for Efficient Solar Hydrogen Production. *Adv. Funct. Mater.* **2025**, *35* (15), 2420912.

(28) Li, T.; Li, Y.; Wang, Y.; Liu, Y.; Liu, Y.; Wang, Z.; Miao, R.; Han, D.; Hui, Z.; Li, W. Neuromorphic Photonics Based on Phase Change Materials. *Nanomaterials* **2023**, *13* (11), 1756.

(29) Tara, V.; Chen, R.; Froch, J. E.; Fang, Z.; Fang, J.; Audhkhasi, R.; Choi, M.; Majumdar, A. Non-Volatile Reconfigurable Transmissive Notch Filter Using Wide Bandgap Phase Change Material Antimony Sulfide. *IEEE J. Sel. Top. Quantum Electron.* **2024**, *30* (4), 1.

(30) Chen, R.; Fang, Z.; Perez, C.; Miller, F.; Kumari, K.; Saxena, A.; Zheng, J. J.; Geiger, S. J.; Goodson, K. E.; Majumdar, A. Non-volatile electrically programmable integrated photonics with a 5-bit operation. *Nat. Commun.* **2023**, *14* (1), 3465.

(31) Gutierrez, Y.; Ovvyan, A. P.; Santos, G.; Juan, D.; Rosales, S. A.; Junquera, J.; Garcia-Fernandez, P.; Dicorato, S.; Giangregorio, M. M.; Dilonardo, E.; et al. Interlaboratory study on Sb_2S_3 interplay between structure, dielectric function, and amorphous-to-crystalline phase change for photonics. *iScience* **2022**, *25* (6), 104377.

(32) Dong, W.; Liu, H.; Behera, J. K.; Lu, L.; Ng, R. J. H.; Sreekanth, K. V.; Zhou, X.; Yang, J. K. W.; Simpson, R. E. Wide Bandgap Phase Change Material Tuned Visible Photonics. *Adv. Funct. Mater.* **2019**, *29* (6), 1806181.

(33) Kepic, P.; Liska, P.; Idesová, B.; Caha, O.; Ligmajer, F.; Sikola, T. Pulsed laser deposition of Sb_2S_3 films for phase-change tunable nanophotonics. *New J. Phys.* **2024**, *26* (1), 013005.

(34) Gao, K.; Qiang, F.; Tian, S.; Tan, Y.; Liu, S.; Zhang, W.; Mei, T. Optimizing Wavelength for Enhanced Cycling Durability of Laser-Induced Phase Change in Sb_2S_3 Films: A Survey on Optical Transmission Phase Shift. *Adv. Opt. Mater.* **2024**, *12* (13), 2302722.

(35) Guo, P.; Sarangan, A. M.; Agha, I. A Review of Germanium-Antimony-Telluride Phase Change Materials for Non-Volatile Memories and Optical Modulators. *Appl. Sci.* **2019**, *9* (3), 530.

(36) George, S. M. Atomic Layer Deposition: An Overview. *Chem. Rev.* **2010**, *110* (1), 111−131.

(37) Xu, H.; Akbari, M. K.; Kumar, S.; Verpoort, F.; Zhuiykov, S. Atomic layer deposition - approach to nanoscale hetero-interfacial engineering of chemical sensors electrodes: A review. *Sens. Actuators, B* **2021**, *331*, 129403.

(38) Hoye, R. L. Z.; Muñoz-Rojas, D.; Sun, Z.; Okcu, H.; Asgarimoghaddam, H.; MacManus-Driscoll, J. L.; Musselman, K. P. Spatial Atomic Layer Deposition for Energy and Electronic Devices. *PRX Energy* **2025**, *4*, 017002.

(39) Bayliss, P.; Nowacki, W. Refinement of the crystal structure of stibnite, Sb_2S_3. *Z. Kristallogr. -Cryst. Mater.* **1972**, *135*, 308−315.

(40) Thompson, C. V. Solid-State Dewetting of Thin Films. *Annu. Rev. Mater. Res.* **2012**, *42*, 399−434.

(41) Niekiel, F.; Kraschewski, S. M.; Muller, J.; Butz, B.; Spiecker, E. Local temperature measurement in TEM by parallel beam electron diffraction. *Ultramicroscopy* **2017**, *176*, 161−169.

(42) Lenthe, W. C.; Singh, S.; De Graef, M. A spherical harmonic transform approach to the indexing of electron back-scattered diffraction patterns. *Ultramicroscopy* **2019**, *207*, 112841.

(43) Singh, S.; Ram, F.; De Graef, M. EMsoft: Open source software for electron diffraction/image simulations. *Microsc. Microanal.* **2017**, *23* (S1), 212−213.